The Viscous Wall-Layer Effect in Injected Porous Pipe Flow

Moshe Ben-Reuven*
Princeton Combustion Research Laboratories, Inc., Monmouth Junction, New Jersey

This analysis is aimed at the near-wall processes in an injected axisymmetric porous pipe flow. It is a part of an overall study of solid-propellant rocket instability, in which cold-flow simulation is evaluated as a tool to elucidate possible instability driving mechanisms. One such prominent mechanism seems to be viscoacoustic coupling, as indicated by earlier, detailed order-of-magnitude analysis. In this study, the viscous wall layer is analyzed at steady state to determine its effect on the flowfield prior to the onset of appreciable turbulence. The formulation is derived in terms of a nonsteady singular boundary-layer problem, with detail (up to second order) given only to the near-wall region. The injection Reynolds number is large and its inverse square root serves as an appropriate small perturbation quantity. The injected Mach number is also small and taken of the same order as the aforesaid small quantity for the present simulation. The radial dependence of the wall-layer solutions up to second order was derived in polynomial form. The first-order axial pressure distribution is solved in terms of a cosine expression, at steady state; this pressure and the associated viscous friction coefficient are shown to agree very well with experimental injected flow data.

Nomenclature

A_t, A = nozzle throat area and port exit area, respectively
a = adiabatic velocity of sound
C_f = wall friction coefficient
C_v, C_p = isochoric and isobaric specific heats, J/kg·K
F = radial mass flux
G = axial mass flux
h = thermal enthalpy
K_m = ratio of inverse Reynolds number and Mach number squared
L = chamber length
M = Mach number
p = pressure
P_r = Prandtl number
R_0^* = channel radius
R_{e0} = injected Reynolds number
r = radial coordinate
$S_{1,2,3}$ = "source" terms in the equations of motion for core flow
S_{RO} = Strouhal number, injected
t = time
U_0 = parameter defining (x,t), variation of wall layer axial velocity component
$u, \bar{u}$ = axial velocity and mean axial core flow velocity, respectively
v = radial velocity component
x = axial distance
y = radial, magnified wall-layer coordinate, perpendicular to surface
γ = C_p/C_v specific heat ratio
Δ = difference, increment
δ = length scales
ϵ = small perturbation quantity
λ = thermal conductivity of gas (air), J/K·m·s
μ = viscosity coefficient, kg/m·s
ρ = density, kg/m^3

Subscripts, Superscripts

0 = zeroth-order (perturbation)
1 = first-order perturbation
( )* = dimensional quantity

Introduction

THIS is part of a study aimed at elucidation of the physical mechanism capable of driving acoustic instability in solid-propellant rocket motors. A particular nonlinear mechanism of interest is termed viscoacoustic coupling, which is expected to prevail in the viscous wall sublayer (or Stokes layer) upstream of the onset of appreciable turbulence. Preliminary analysis has indicated that the viscoacoustic mechanism is sufficiently powerful to drive nonlinear vibrations; it has been shown that the frequency-dependent surface heat-transfer component (due to this coupling) can obtain both phase and amplitude ranges that might drive acoustic vibrations with a solid-propellant wall.

The present study is therefore motivated by particular nonsteady features of this internal flow family. As a necessary initial step, certain properties of the viscous wall layer are investigated at steady state. The objectives are to demonstrate the validity of the physical approach and model through comparison with available experimental data, and to evaluate the injected porous tube cold-flow device as a simulation tool for internal rocket flows. In both instances, the availability of reliable steady-state experimental data is advantageous.

Background

Culick[1] derived a solution to the Stokes stream function equation for flow in a pipe with injected sidewalls. The flow was rotational and, despite being inviscid, could obtain a solution for the axial velocity component that satisfied the no-slip boundary condition at the wall. The solution, which satisfies the boundary data, namely, $u(x=0)=0$, $u(r=1)=0$, and $v(r=1)=-1$, yields

$$v = -\sin\left(\frac{\pi}{2}r^2\right)\Big/ r$$

$$u = \pi x \cos\left(\frac{\pi}{2}r^2\right)$$

Presented as Paper 84-0289 at the AIAA 22nd Aerospace Sciences Meeting, Reno, NV, Jan. 9-12, 1984; received Jan. 19, 1984; revision received May 8, 1985.

*Research Scientist; currently President, MBR Research, Inc., Princeton, NJ. Member AIAA.

Of the general family of solutions obtainable, only that allowing full determination of the vorticity (the azimuthal component alone remains), by the available boundary data, is physically meaningful; the rest were therefore rejected. The axial pressure distribution obtained from the momentum equation is parabolic,

$$[p^*(0)-p^*(x)]/\tfrac{1}{2}\rho^* v_0^{*2}=(\pi\chi)^2$$

This type of injected flowfield has been previously investigated both experimentally and theoretically. In particular, the early theoretical work of Berman,[2] who arrived at a power series solution to the perturbation problem of suction in a flat, porous-walled channel, with the inverse of the suction Reynolds number serving as small-perturbation quantity. The analytical results of Taylor[3] and Wageman and Guevara[4] more closely resemble the cosine terms of Culick[1]; both have carried out experiments as well and both demonstrated very good agreement between the measured axial velocity profiles and the calculated ones. It appears that Culick arrived at his results independently, since no reference was made to any of the previous works. In the experiments by Dunlap et al.,[5] the formulation derived by Culick was used to correlate the measured data, again with considerable success, regarding the core flow axial velocity profile, that is, away from the close neighborhood of the wall.

Other experiments by Olson and Eckert[6] and later by Huesman and Eckert[7] likewise tend to verify the validity of this formulation, in particular regarding the radial velocity profile, which indeed exhibits a peak near the porous surface,[6] as well as the axial pressure distribution (the latter shown as a linear correlation between the friction coefficient C_f and the inverse mean axial velocity, which are both proportional to $1/x$.

The recent experimental study by Brown et al.[8] provides valuable information regarding the steady-state axial pressure profile and the axial velocity distribution, as well as nonsteady wall heat transfer (obtained by exciting the standing acoustic modes in the tube). Departure of the steady-state pressure distribution data from the predictions of the aforementioned formulation by Culick[1] was attributed to the possible transition to turbulence. As will be shown in this study, the pressure data obtained can be simulated very well with a first-order pressure perturbation arising from the laminar viscous wall-layer analysis.

Earlier, Yagodkin[9] reported an experimental cold-flow setup, with an injected porous pipe. The maximal injection Reynolds number was 250, which is two to three orders of magnitude less than that corresponding to actual internal rocket flows. Hot-wire anemometry was used to obtain axial velocity and axial velocity fluctuation vs axial and radial distance. Turbulence intensity seems to peak near the surface and decrease toward the centerline and toward the pipe wall. These observations are qualitatively similar to those obtained later by Yamada et al.[10] Although a transition region, at $R_{e0}=100$-150, was speculated[9] to involve "large eddy structures," no such evidence appears in the experimental data reported in Ref. 9.

Further studies by Yagodkin, with Varapaev[11] and Sviridenkov,[12] are theoretical and address the problem of laminar stability of injected channel flows, i.e., transition to turbulence. Thus, modified versions of the Orr-Sommerfield problem were investigated analytically[11] and numerically.[12] Two related laminar flow stability analyses are by Goldshtik and Sapozhnikov[13] and Alekseev and Korotkin.[14] None of these theoretical analyses indicates the presence of large turbulent eddy structures prior to a full transition point; neither do they obtain an origin of such turbulence on the centerline upstream.

Recently, Flandro[15] carried out a theoretical analysis for a burning propellant in a cylindrical grain under the effect of incident acoustic waves. A detailed formulation was derived with a double expansion, in terms of both inverse Reynolds number and Mach number (independent small parameters). A nonsteady premixed combustion zone was considered near the propellant surface; the assumption was made, however, that flow within the combustion zone is pure radial, i.e., zero axial component to all orders. Thus, it could be anticipated that the results would resemble (regarding nonsteady combustion behavior) those of T'ien,[16] and there seem to be only small differences between the response to tangent and perpendicular wave incidence. The problem was finally solved numerically and details of the inner/outer matching process were not given.

In the remainder of this paper, the viscous, injected wall-layer formulation is derived in perturbation form. Analytical near-field solutions are obtained for all variables up to first order (inclusive) regarding the radial coordinate dependence; the remaining (x,t) dependence is shown to be governed by a relatively simple partial differential system. These solutions are discussed, with particular attention to the resultant steady-state pressure distribution and wall shear stress for which experimental data are available.

Analysis

Analytical Model of the Core Flow

The equations of motion pertaining to the core flow are presented, for an axisymmetric flowfield. The objective is to simulate the cold-flow experiments of Brown at UTC/CSD, which utilize cylindrical geometry. For the core flow region, with typical injection Reynolds numbers of order 10^4, constant and uniform thermophysical properties were assumed. A schematic of the physical configuration is shown in Fig. 1. Turbulence and combustion are precluded from the present formulation. Other than these simplifications, the full compressible, nonsteady, viscous equations of motion are considered, with all the dissipative terms included.

The five equations of motion, for continuity, radial momentum, axial momentum and energy are presented in differential form. A caloric equation of state (pertaining to perfect gas) completes the model to form closure of the dependent variables.

The following dimensionless independent variables are introduced, based on the two physical scales of reference, namely, inner chamber radius R_0^* and reference injection velocity v_0^*:

$$r=r^*/R_0^*,\quad x=x^*/R_0^*,\quad t=t^*/t_0^* \tag{1}$$

where $t_0^*=R_0^*/v_0^*$.

The dependent variables are

$$v=v^*/v_0^*,\quad u=u^*/v_0^*$$

$$\rho=\rho^*/\rho_0^*,\quad h=h^*/h_0^*,\quad p=p^*/p_0^* \tag{2}$$

The properties used for nondimensionalization are the reference (injected) density ρ_0^* and the reference chamber pressure p_0^*; the corresponding thermal enthalpy h_0^* is calculated from the caloric equation of state,

$$p_0^*=\frac{\gamma-1}{\gamma}\rho_0^* h_0^* \tag{3}$$

where $\gamma=C_p/C_v$ the specific heat ratio, is considered a constant. The reference speed of sound is

$$a_0^*=(\gamma p_0^*/\rho_0^*)^{1/2}=\sqrt{(\gamma-1)h_0^*} \tag{4}$$

The corresponding injection Mach number is

$$M_0=v_0^*/a_0^* \tag{5}$$

The reference (injection) Reynolds number and Prandtl number are, respectively,

$$R_{e0}=\frac{\rho_0^* v_0^* R_0^*}{\mu}, \quad P_r=\frac{\mu C_p}{\lambda} \tag{6}$$

Recall that the viscosity, thermal conductivity, and isobaric specific heat are all uniform and constant within the present cold-flow simulation. These idealizations are incorporated merely for convenience in allowing clear identification of physical interactions within the core flow at low (axial) Mach numbers; sharp pressure and temperature variations are obviously precluded. The dimensionless equations of motion are as follows for the region $0<x<L$, $0<r<1$, $t>0$:

$$\frac{\partial \rho}{\partial t}+\frac{1}{r}\frac{\partial}{\partial r}(r\cdot\rho v)+\frac{\partial \rho u}{\partial x}=0 \tag{7}$$

$$\frac{\partial \rho v}{\partial t}+\frac{1}{r}\frac{\partial}{\partial r}(r\cdot\rho v^2)+\frac{\partial \rho v u}{\partial x}=S_2 \tag{8}$$

$$\frac{\partial \rho u}{\partial t}+\frac{1}{r}\frac{\partial}{\partial r}(r\cdot\rho u v)+\frac{\partial}{\partial x}\left(\rho u^2+\frac{P}{\gamma M_0^2}\right)=S_3 \tag{9}$$

$$\frac{\partial \rho h}{\partial t}+\frac{1}{r}\frac{\partial}{\partial r}(r\cdot\gamma\rho h v)+\frac{\partial}{\partial x}(\gamma\rho h u)=S_4 \tag{10}$$

The right-hand side (source) terms are defined as

$$S_2=\frac{4/3}{R_{e0}}\frac{1}{r}\left(\frac{\partial v}{\partial r}-\frac{v}{r}\right)-\frac{1}{\gamma M_0^2}\frac{\partial p}{\partial r}+\left[\frac{\partial^2 v}{\partial x^2}+\frac{1}{3}\frac{\partial}{\partial r}\left(\frac{\partial u}{\partial x}+4\frac{\partial v}{\partial r}\right)\right]\Big/R_{e0} \tag{11}$$

$$S_3=\frac{1/r}{R_{e0}}\left(\frac{\partial u}{\partial r}+\frac{1}{3}\frac{\partial v}{\partial x}\right)+\left[\frac{\partial^2 u}{\partial r^2}+\frac{1}{3}\frac{\partial}{\partial x}\left(\frac{\partial u}{\partial x}+\frac{\partial v}{\partial r}\right)\right]\Big/R_{e0} \tag{12}$$

$$S_4=\gamma\left(v\frac{\partial p}{\partial r}+u\frac{\partial p}{\partial x}\right)+\frac{\gamma/P_r}{R_{e0}}\left(\frac{1}{r}\frac{\partial h}{\partial r}+\frac{\partial^2 h}{\partial r^2}+\frac{\partial^2 h}{\partial x^2}\right)+\gamma(\gamma-1)M_0^2\left\{\frac{4}{3}\left[\left(\frac{\partial u}{\partial x}\right)^2+\left(\frac{\partial v}{\partial r}\right)^2+\left(\frac{v}{r}\right)^2\right]-\frac{4}{3}\left[\left(\frac{\partial v}{\partial r}-\frac{v}{r}\right)\frac{\partial u}{\partial x}+\frac{v}{r}\frac{\partial v}{\partial r}\right]+\left(\frac{\partial u}{\partial r}+\frac{\partial v}{\partial x}\right)^2\right\}\Big/R_{e0} \tag{13}$$

The following physical boundary data are available,

1) On the center line (t, $r=0$, x),

$$v=0, \quad \frac{\partial u}{\partial r}=0, \quad \frac{\partial p}{\partial r}=0, \quad \frac{\partial h}{\partial r}=0 \tag{14}$$

2) At the porous (injected) surface (t, $r=1$, x):

$$v=-v_0(x,t), \quad u=0, \quad h=h_0(x,t) \tag{15}$$

3) At the (nonpermeable, solid) head-end closure ($t,r,x=0$),

$$v=0, \quad u=0, \quad h=h_H(r,t) \tag{16}$$

The functions $v_0(x,t)$, $h_0(x,t)$, and $h_H(r,t)$ are arbitrary imposed distributions.

4) The exit plane, defined by (t, r, $x=L$), forms an entrance into a short, convergent nozzle section.

Injected Sidewall Layer

The flow region of interest (Fig. 2) is close to the surface, where viscous forces are expected to be appreciable within a thin layer. For the neighborhood of $r=1$, the following transform is proposed for the radial coordinate:

$$y=(1-r)/\epsilon \tag{17}$$

which magnifies the wall layer, with

$$0<\epsilon\equiv 1/\sqrt{R_{e0}}\ll 1 \tag{18}$$

Thus,

$$\frac{\partial}{\partial r}=-\frac{1}{\epsilon}\frac{\partial}{\partial y}, \quad \frac{\partial^2}{\partial r^2}=\frac{1}{\epsilon^2}\frac{\partial^2}{\partial y^2} \tag{19}$$

and $r=1-\epsilon y$. The assumption of small injection Mach number is constrained as follows. Obviously, the injection Mach number is an additional independent parameter in the formulation (equations of momentum and energy). In the flow types of interest for simulation herein, M_0 is also very small; in consideration of the typical experimental configurations used by Brown,[8]

$$M_0^2\sim\mathcal{O}(1/R_{e0})\sim\mathcal{O}(\epsilon^2)$$

which adequately represents a range of cold-flow conditions. This offers great simplification in the analysis, although at the cost of a narrower range of general application (considering the relative freedom of the two major flow parameters, R_{e0} and M_0). Therefore, a parameter is introduced,

$$K_m\equiv\frac{1/R_{e0}}{\gamma M_0^2}=\frac{\epsilon^2}{\gamma M_0^2}=\text{const} \tag{20}$$

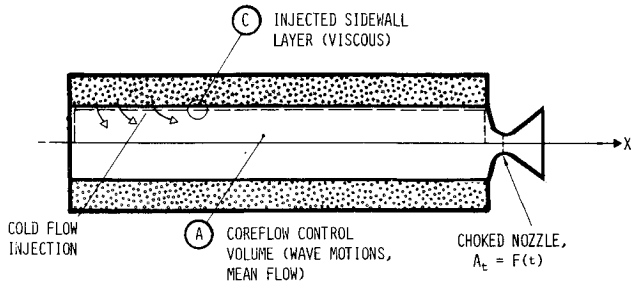

Fig. 1 Simulated axisymmetric, internal rocket chamber flow, showing specific regions of interest.

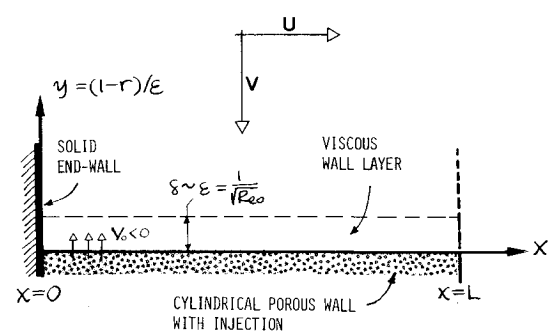

Fig. 2 Injected wall-layer region, showing the perturbed (expanded) "inner" coordinate (the "outer" core flow regime is above, toward the centerline).

The relevant time scale depends on the frequency range of interest. For the flow regime and acoustic perturbation frequencies of interest eventually, the injection Strouhal number is of order unity,

$$S_{RO} = f_0^* R_0^* / v_0^* \tag{21}$$

where f_0 is a reference frequency. Therefore, the viscous sublayer thickness and Stokes layer thickness are also comparable.

$$[R_0^*/\sqrt{R_{e0}}]/[\mu^*/\rho_0^* f_0^*]^{1/2} = \sqrt{S_{RO}} \sim \mathcal{O}(1) \tag{22}$$

Thus, the same time scale used herein for both the viscous sublayer and the main (core) flow can be utilized for nonsteady analysis.

The independent variables are (x,y,t), while the associated dependent variables, in the wall layer, are perturbed,

$$\rho = \rho_0 + \epsilon\rho_1, \quad v = v_0 + \epsilon v_1,$$

$$u = u_0 + \epsilon u_1, \quad h = h_0 + \epsilon h_1 \tag{23}$$

while the following abbreviations are introduced,

$$F_0 \equiv \rho_0 v_0, \quad F_1 \equiv \rho_0 v_1 + \rho_1 v_0$$

$$G_0 \equiv \rho_0 u_0, \quad G_1 \equiv \rho_0 u_1 + \rho_1 u_0$$

$$p_0 \equiv \rho_0 h_0, \quad p_1 \equiv \rho_0 h_1 + \rho_1 h_0 \tag{24}$$

It should be stressed that the $\mathcal{O}(\epsilon)$ terms represent perturbation quantities that may later be considered as series expansions. The present analysis is concerned with the two lowest orders only. This in no way implies limitation to so-called "linear" considerations.

For the perturbation variables of Eqs. (17-24), the continuity equation yields

$$\frac{\partial}{\partial t}(\rho_0 + \epsilon\rho_1) - \frac{1}{\epsilon}\frac{\partial}{\partial y}(F_0 + \epsilon F_1 + \epsilon^2 \rho_1 v_1) + \frac{\partial}{\partial x}(G_0 + \epsilon G_1) = -(1+\epsilon y)(F_0 + \epsilon F_1) \tag{25}$$

Similar substitution of perturbed variables is also carried out for the remaining equations of motion. A hierarchy of equations can then be collected, for equal powers of the small quantity ϵ.

The lower-order analysis (concerning negative powers of ϵ) readily yields the following simple results:

$$F_0 = F_0(x,t), \quad v_0 = v_0(x,t)$$

$$p_0 = p_0(t), \quad p_1 = p_1(x,t) \tag{26}$$

Also, the following differential equation arises from the axial momentum balance at order $1/\epsilon$:

$$K_m \frac{\partial p_1}{\partial x} - \frac{\partial}{\partial y}(F_0 u_0) = 0 \tag{27}$$

which can be integrated to reveal the y dependence of u_0,

$$u_0(x,t;y) = \frac{K_m}{F_0}\left(\frac{\partial p_1}{\partial x}\right) y \tag{28}$$

with

$$u_0(x,t;0) = 0$$

Of course, the (x,t) dependence of u_0 still remains to be found. However, *its dependence upon the layer coordinate y is found to be linear*; this result has several important implications. The axial shear stress component within the layer,

$$\tau_{xy}^0 \sim \frac{\partial u_0}{\partial y} = \frac{K_m}{F_0}\frac{\partial p_1}{\partial x} \tag{29}$$

is obviously nonzero in general, while being independent of distance from the wall at any given position (x,t). Even more striking is the vanishing of the viscous dissipation term at zeroth order,

$$\partial^2 u_0 / \partial y^2 = 0$$

which leaves in the zeroth-order axial momentum equation a balance of inertial terms, strictly. This physically explains the success (up to first order) of modeling this family of injected flows by assuming rotational, inviscid motions; such modeling indeed obtains solutions for the axial velocity profile that satisfy the no-slip condition at the wall ($r=1$). Note that the cosine expression obtained by Culick[1] for the axial velocity also has a leading term proportional to y, upon expansion for small $(1-r)$ at the wall. This consistency indicates that inner/outer matching should be feasible.

It further appears that the shear stress [Eq. (29)] is proportional to the first-order axial pressure gradient, while being inversely proportional to the injected mass flux—as would be expected. Of course, $\partial p_1/\partial x$ depends on F_0; so, one expects their ratio to be finite at the limit as zero injection is approached.

The zeroth-order differential system reads

$$\frac{\partial \rho_0}{\partial t} + \frac{\partial G_0}{\partial x} - \frac{\partial F_1}{\partial y} = -F_0 \tag{30}$$

$$\frac{\partial F_0}{\partial t} + \frac{\partial}{\partial x}(F_0 u_0) - \frac{\partial}{\partial y}(F_0 v_1 + F_1 v_0) = -F_0 v_0 + \frac{4}{3}\frac{\partial^2 v_0}{\partial y^2} \tag{31}$$

$$\frac{\partial G_0}{\partial t} + \frac{\partial G_0 u_0}{\partial x} - \frac{\partial}{\partial y}(G_0 v_1 + G_1 v_0) = -G_0 v_0 + \frac{\partial^2 u_0}{\partial y^2} \tag{32}$$

$$\frac{\partial p_0}{\partial t} + \frac{\partial}{\partial x}(\gamma p_0 u_0) - \frac{\partial}{\partial y}(\gamma p_1 v_0 + \gamma p_0 v_1) = -\gamma p_0 v_0 + (\gamma - 1)\left[u_0 \frac{\partial p_0}{\partial x} - \left(v_1 \frac{\partial p_0}{\partial y} + v_0 \frac{\partial p_1}{\partial y}\right)\right] + \frac{\gamma}{P_r}\frac{\partial^2 h_0}{\partial y^2} \tag{33}$$

The corresponding first-order formulation is

$$\frac{\partial \rho_1}{\partial t} + \frac{\partial G_1}{\partial x} - \frac{\partial \rho_1 v_1}{\partial y} = -F_1 - yF_0 \tag{34}$$

$$\frac{\partial F_1}{\partial t} + \frac{\partial}{\partial x}(F_0 u_1 + F_1 u_0) - \frac{\partial}{\partial y}[v_1(F_1 + \rho_1 v_0)] = -[F_0 v_0 y + (F_0 v_1 + F_1 v_0)] + \frac{4}{3}\frac{\partial^2 v_1}{\partial y^2} + \frac{4}{3}\frac{\partial v_0}{\partial y} - \frac{1}{3}\frac{\partial^2 u_0}{\partial x \partial y} \tag{35}$$

$$\frac{\partial G_1}{\partial t}+\frac{\partial}{\partial x}(G_1u_0+G_0u_1)-\frac{\partial}{\partial y}(G_1v_1+\rho_1v_0u_1)$$

$$=-(G_1v_0+G_0v_1)-G_0v_0y+\frac{\partial^2u_1}{\partial y^2}-\frac{\partial u_0}{\partial y}-\frac{1}{3}\frac{\partial^2v_0}{\partial x\partial y} \quad (36)$$

$$\frac{\partial p_1}{\partial t}+\frac{\partial}{\partial x}(\gamma p_1u_0+\gamma u_1p_0)-\frac{\partial}{\partial y}(\gamma p_1v_1)=-\gamma p_0v_0y$$

$$-\gamma(p_0v_1+p_1v_0)+\frac{\gamma}{P_r}\left(-\frac{\partial h_0}{\partial y}+\frac{\partial^2h_1}{\partial y^2}\right)$$

$$+(\gamma-1)\left(u_1\frac{\partial p_0}{\partial x}+u_0\frac{\partial p_1}{\partial x}-v_1\frac{\partial p_1}{\partial y}\right) \quad (37)$$

With the foregoing result for axial velocity, the zeroth-order formulation can be utilized to solve for the y dependence of the other dependent variables. The zeroth-order continuity equation can be written in split form, since F_0 and ρ_0 are independent of y,

$$\frac{\partial\rho_0}{\partial t}+F_0(x,t)=C_0(x,t) \quad (38)$$

$$\frac{\partial}{\partial x}\left(\frac{K_m}{v_0}\frac{\partial p_1}{\partial x}\right)y-\frac{\partial F_1}{\partial y}=-C_0(x,t) \quad (39)$$

where $C_0(x,t)$ is a common separation parameter with a range of values uniquely corresponding to the boundary data. The second equation yields

$$F_1(y,x,t)=B_0(x,t)+C_0(x,t)y+\frac{1}{2}\frac{\partial}{\partial x}(\rho_0U_0)y^2 \quad (40)$$

where:

$$B_0(x,t)=F_1(0,x,t) \quad (41)$$

$$U_0(x,t)\equiv\frac{K_m}{F_0}\frac{\partial p_1}{\partial x} \quad (42)$$

Similarly, the zeroth-order radial momentum equation yields, after splitting:

$$\frac{\partial F_0}{\partial t}+F_0v_0=C_1(x,t) \quad (43)$$

$$v_1(x,t;y)=B_1(x,t)+\frac{C_1-v_0C_0}{F_0}y+\frac{1}{2}U_0\cdot\frac{1}{v_0}\frac{\partial v_0}{\partial x}y^2$$

$$B_1(x,t)=v_1(x,t;0) \quad (44)$$

The foregoing results for F_1 and v_1 yield the first-order density:

$$\rho_1(x,t;y)=\frac{(B_0-\rho_0B_1)}{v_0}+\frac{(2C_0-C_1/v_0)}{v_0}y+\frac{\partial}{\partial x}\left(\frac{\rho_0U_0}{v_0}\right)\cdot\frac{y^2}{2}$$

(45)

Note that: $\rho_1(0,x,t)=(B_0-\rho_0B_1)/v_0$ so that ρ_1 is uniquely defined and no additional integration is necessary. Now, following the definition of p_1 in Eq. (24),

$$h_1(y;x,t)=[p_1-h_0\rho_1(y;x,t)]/\rho_0 \quad (46)$$

Note that although $p_0=p_0(t)$, the zeroth-order enthalpy $h_0(x,t)$ may still obtain a nonuniform axial temperature distribution.

The axial momentum balance [Eq. (32)], after dividing through by F_0 and following integration yields

$$u_1(x,t;y)=\frac{U_0}{F_0}\left[\rho_0\frac{\partial U_0}{\partial x}-\frac{1}{2}\frac{\partial}{\partial x}(\rho_0U_0)\right]\frac{y^3}{3}$$

$$+\left(\frac{1}{v_0}\frac{\partial U_0}{\partial t}-\frac{C_0U_0}{F_0}\right)\frac{y^2}{2}-\frac{B_0U_0}{F_0}y \quad (47)$$

so that $u_1(0,x,t)=0$, satisfying the no-slip condition at the wall. Thus, the perturbed axial velocity is third order in its y dependence and the corresponding viscous dissipation term (unlike its zeroth-order counterpart) does not vanish at the wall.

Having determined already that $p_0=p_0(t)$ in general (through lower-order analysis), the zeroth-order energy equation is not expected to yield any further information useful for steady-state analysis and is therefore discarded. One may turn now to the first-order energy equation, which seems to yield some simple and highly useful results even without full solution. After some manipulation, Eq. (37) obtains

$$\frac{\partial p_1}{\partial t}+\gamma p_1\left(\frac{\partial u_0}{\partial x}-\frac{\partial v_1}{\partial y}+v_0\right)+\gamma p_0\left(\frac{\partial u_1}{\partial x}+v_0y+v_1\right)$$

$$+u_0\frac{\partial p_1}{\partial x}-\frac{\gamma}{P_r}\frac{\partial^2h_1}{\partial y^2}=0 \quad (48)$$

Using the appropriate first-order expressions obtained earlier (for u_1, v_1, and h_1) in Eq. (48) and collecting equal powers of y yields

$$\left\{\frac{\partial p_1}{\partial t}+\gamma p_1\left(v_0-\frac{C_1-C_0v_0}{F_0}\right)\right.$$

$$\left.+\gamma p_0\left[B_1+\frac{1/P_r}{\rho_0^2}\frac{\partial}{\partial x}\left(\frac{\rho_0U_0}{v_0}\right)\right]\right\}y^0$$

$$+\left\{\gamma p_1v_0\frac{\partial}{\partial x}\left(\frac{U_0}{v_0}\right)+\gamma p_0\left[\frac{\partial}{\partial x}\left(-\frac{U_0B_0}{F_0}\right)\right.\right.$$

$$\left.\left.+v_0+\frac{C_1-C_0v_0}{F_0}\right]+U_0\frac{\partial p_1}{\partial x}\right\}y$$

$$+\gamma p_0\left[\frac{U_0}{v_0}\frac{\partial v_0}{\partial x}+\frac{\partial}{\partial x}\left(\frac{1}{v_0}\frac{\partial U_0}{\partial t}-\frac{C_0U_0}{F_0}\right)\right]\frac{y^2}{2}$$

$$+\frac{\partial}{\partial x}\left[\frac{U_0}{v_0}\cdot\frac{\rho_0}{2}\cdot\frac{\partial}{\partial x}\left(\frac{U_0}{\rho_0}\right)\right]\frac{y^3}{3}=0 \quad (49)$$

Compatibility with the foregoing derivation [in which y and (x,t) variable separation was implemented] can be maintained provided each of the bracketed terms in Eq. (49) vanishes identically. The resulting four compatibility relations would, in principle, determine the behavior of the wall sublayer system up to the first order in ϵ, the small perturbation quantity. A total of three undetermined coefficients should arise necessarily to accommodate coupling with the outer, inviscid (core) flowfield, through inner/outer asymptotic matching.

First-Order Pressure Perturbation

In this section, the first-order axial pressure distribution at steady state will be resolved, based on the viscous wall-layer formulation derived earlier. Before carrying out this derivation, however, several physical aspects of the injected

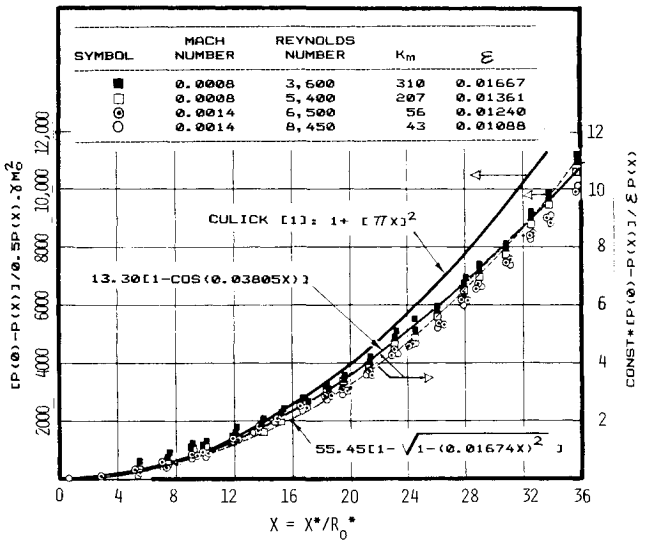

Fig. 3 Dimensionless axial pressure distribution. Shown are the experimental points of Brown et al.[8] with their original scale at left, along with the rotational-inviscid solution by Culick.[1] The two first-order solutions generated from the present viscous sublayer analysis are overplotted.

flowfield should be discussed from the viewpoint of the "outer" inviscid core flow region.

In the outer inviscid core flow, the axial pressure difference is balanced by the appropriate flow acceleration, so that

$$[p^*(0)-p^*(x)]/(\tfrac{1}{2}\rho_0^*\bar{u}^{*2}) \sim \mathcal{O}(1) \tag{50}$$

In contrast, the seemingly equivalent dimensionless representation by Brown et al.[8] in which the mean axial velocity is replaced by the injection Mach number,

$$\frac{[p^*(0)-p^*(x)]}{\tfrac{1}{2}\gamma p^*(x)M_0^2} \sim \left(\frac{L^*}{R_0^*}\right)^2 \gg 1 \tag{51}$$

indeed obtains large numbers for large values of $x=x^*/R_0$, as shown in Fig. 3. The last proportionality was obtained from the overall conservation of mass within the injected tube. Typically, $L^*/R_0 \sim \mathcal{O}(10)$ in the aforesaid experiments.[8] In agreement with the typical injection Reynolds numbers of this experimental setup, suppose now that

$$(L^*/R_0^*)^2\epsilon \sim (L^*/R_0^*)^2 M_0 \sim \mathcal{O}(1) \tag{52}$$

where $0<\epsilon\ll 1$ is the small-perturbation quantity defined by Eq. (18). Thus, dividing the left side of Eq. (51) by that of Eq. (50), one obtains the velocity ratio,

$$\bar{u}^*_{(\text{outer})}/v^*_{0\ (\text{inject})} \sim \mathcal{O}(1/\sqrt{\epsilon}) \tag{53}$$

Furthermore, using the last proportionality of Eq. (52) in Eq. (51), the dimensionless axial pressure difference is

$$[p^*(0)-p^*(x)]/p^*(x) \sim M_0 \sim \mathcal{O}(\epsilon) \tag{54}$$

Obviously, one may now generate a variety of injected Mach numbers with the same porous tube having a fixed length/diameter ratio. To avoid ambiguity, the L^* herein should be viewed as a reference axial length that satisfies Eqs. (51) and (52), of the same order of magnitude as (but not fixed as) the geometrical tube length. The physical significance of this definition can be demonstrated by Eq. (51): whenever injecting at a very small M_0, a rather large L^* is needed to detect an appreciable axial pressure drop.

Recall that $p_0=p_0(t)$ and $p_1=p_1(x,t)$ as derived in the wall-layer analysis. Hence, up to first order, no radial pressure gradients arise, and the "inner" and "outer" pressures must be equal, viz.,

$$p_0^{(o)}=p_0^{(i)}, \quad p_1^{(o)}=p_1^{(i)} \tag{55}$$

Suppose now that the leading term in the outer axial velocity expansion is, according to Eq. (53),

$$u^{(o)}(x,r,t) \sim \frac{u_{-1}^{(o)}}{\sqrt{\epsilon}} + u_0^{(o)} + \text{h.o.t.} \tag{56}$$

(h.o.t = higher order terms), while the remaining outer variables are of simpler form, e.g.,

$$v^{(o)}(x,r,t) \sim v_0^{(o)} + \sqrt{\epsilon}v_1^{(o)} + \text{h.o.t.}$$

Therefore, the outer axial momentum balance, derived from Eqs. (7-12) yields, at order $1/\epsilon$,

$$\frac{\partial}{\partial x}(\rho_0^{(o)}u_{-1}^{(o)}u_{-1}^{(o)} + K_m p_1^{(o)}) = 0 \tag{57}$$

which demonstrates the actual manner by which the first-order pressure perturbation is supported in the outer core flow.

To conclude, a first-order pressure perturbation within the flowfield, $\epsilon p_1(x,t)$, has been postulated, following the viscous wall-layer analysis. The pressure is common to both inner (wall-layer) and outer (core flow) regions. Within the wall layer, it is balanced by the shear force, or zeroth-order vorticity generation, as shown in Eq. (27). In the core flow, it is balanced by the lowest-order axial acceleration.

As evident in Fig. 3, the experimental data of Brown et al.[8] also demonstrates that significant departures from the parabolic axial pressure drop profile (as predicted by the inviscid formulation) evolve at sufficiently large x. In the meantime, departures from the self-similar cosine velocity profiles are evident, which become more appreciable with increasing x. Therefore, elucidation of the first-order pressure perturbation seems to be very important for proper understanding of this type of injected flow. This is undertaken in the remainder of the present section for steady state.

Axial Pressure Distribution

Either of the first two compatibility conditions of Eq. (49) can be used to solve for the axial distribution of $p_1(x)$; we begin with the first condition (the one independent of y). At steady state, the time derivative drops and, from Eqs. (38) and (43), $C_1=v_0C_0$, so that the equation reads

$$\gamma p_1 v_0 + \gamma p_0\left[B_1 + \frac{1/P_r}{\rho_0^2}\frac{\mathrm{d}}{\mathrm{d}x}\left(\frac{\rho_0 U_0}{v_0}\right)\right] = 0 \tag{58}$$

where B_1 is the value of the injection velocity perturbation at the wall, defined by Eq. (44), and U_0 is defined by Eq. (42). Let

$$v_0=F_0=-1 \text{ and } p_0=\rho_0=1 \tag{59}$$

which are uniform distributions. Note that the negative signs of F_0 and v_0 denote injection at the wall, while positive signs denote suction. The radial velocity perturbation at the wall is expressed as

$$B_1=\alpha_0+\alpha_1 p_1(x) \tag{60}$$

where the second term anticipates the response to the local pressure perturbation; both coefficients are expected to be

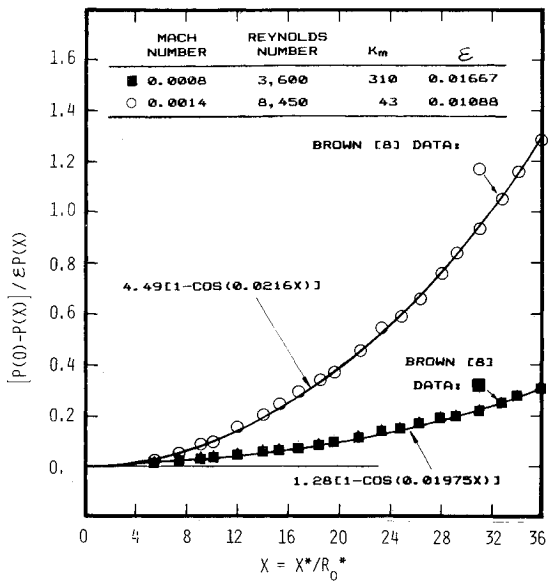

Fig. 4 Sensitivity of the measured axial pressure drop to the injection Reynolds and Mach numbers (or to the parameters K_m and ϵ) is demonstrated after rescaling two distinct data groups from Fig. 3. Excellent correlations are obtained by the use of the cosine solution obtained herein. The increasing vertical "dispersion" of the data points (with increasing x) in Fig. 3 is thus explained physically and is not due to an increasing error in measurement.

positive. Now the first compatibility equation reads

$$\frac{d^2p_1}{dx^2} + b_1^2 p_1 = -b_0 \qquad 0<x<L \tag{61}$$

where

$$b_0 \equiv \alpha_0 P_r/K_m, \quad b_1 \equiv [P_r(\alpha_1 - 1)/K_m]^{1/2} \tag{62}$$

The boundary data are

$$dp_1/dx(0) = 0, \quad p_1(L) = p_L \tag{63}$$

The solution to the two-point boundary value problem is

$$p_1(x) = A_1 \cos(b_1 x) - b_0/b_1^2 \tag{64}$$

Interestingly, the second compatibility condition of Eq. (49), the one proportional to y, obtains a family of boundary value problems for $p_1(x)$ quite different from the harmonic [Eq. (61)]. The solution is as follows. After use of the same assumptions as in Eq. (59), the second compatibility condition yields

$$p_1 \frac{d^2p_1}{dx^2} + \frac{d}{dx}\left(B_0 \frac{dp_1}{dx}\right) + \frac{1}{K_m} + \frac{1}{\gamma}\left(\frac{dp_1}{dx}\right)^2 = 0 \tag{65}$$

where B_0 is the radial mass flux perturbation at the wall defined by Eq. (41). This is expressed similarly to B_1 as

$$B_0 = \beta_0 + \beta_1 p_1(x) \tag{66}$$

After some manipulation, the nonlinear differential equation is, for $0<x<L$,

$$(\lambda_2 + \lambda_1 p_1)\frac{d^2p_1}{dx^2} + \left(\frac{dp_1}{dx}\right)^2 + \lambda_0 = 0$$

$$\lambda_0 \equiv \frac{1/K_m}{(1/\gamma)+\beta_1}, \quad \lambda_1 \equiv \frac{1+\beta_1}{(1/\gamma)+\beta_1}, \quad \lambda_2 \equiv \frac{\beta_0}{(1/\gamma)+\beta_1} \tag{67}$$

A general solution will not be attempted herein; however, the approximation for $\beta_1 \gg 1$,

$$\lambda_1 \simeq 1$$

yields a solution that satisfies the boundary data of Eq. (63),

$$p_1(x) = -\lambda_2 + \left(\frac{b_2}{\lambda_0}\right)^{1/2}[1-(b_4 x)^2]^{1/2} \tag{68}$$

where $b_4 \equiv \lambda_0/(b_2)^{1/2}$ and b_2 is an integration constant. It will be shown that both Eqs. (64) and (68) correlate the available experimental axial pressure drop data very well, with very small differences between the numerical values generated.

In summary, two solutions to the axial pressure distribution are obtained, as a result of the viscous wall-layer analysis. Both solutions depend critically upon the perturbed wall-injection velocity B_1 or mass flux B_0.

The parts of these perturbation parameters (α_0 and β_0), which are independent of pressure, represent a uniform injection correction. These two parameters affect the eigenvalue of each of the compatibility equations, b_0 and λ_2, which, in particular, determines whether satisfying a downstream boundary condition is feasible.

The pressure-dependent parts α_1 and β_1 represent the real part of the complex pressure response (or admittance) functions of the porous wall material. Significantly, both are positive, which means that the porous material behaves in a manner similar to that of an orifice (increase inward injection rate when inner pressure drops), as expected; this is the opposite of a typical propellant response (where the enhanced burning rate is caused by an inner pressure increase). The two pressure-dependent parameters affect the inverse axial wavelength characteristic of the frictional or viscous pressure drop; the respective parameters are b_1 in Eq. (64) and b_4 in Eq. (68).

Interestingly, if the sign of $(b_1)^2$ is reversed in Eq. (61), as for $\alpha_1<0$ representing propellant-like admittance, a family of hyperbolic solutions would be obtained. A hyperbolic cosine can accommodate the boundary data of Eq. (63) and the axial pressure drop, but its steep variation can only poorly simulate the injected cold-flow data of Brown et al.[8] From these considerations, some of the difficulties in the simulation of internal rocket flow by porous-pipe injected flow may be indicated, particularly regarding the axial development of the vorticity in the wall layer inferred from the axial pressure drop.

Discussion of Results

According to Eq. (54), the normalized axial pressure drop is defined, using the distribution obtained by Eq. (64), as

$$\Delta p_1 \equiv \frac{p(0)-p(x)}{\epsilon p(x)} = A_1(1-\cos b_1 x) + \mathcal{O}(\epsilon) \tag{69}$$

This formula is used to correlate the experimental data of Brown et al.,[8] as shown in Fig. 3. Clearly, the measured pressure drop profile is correlated very well by Eq. (69), which is obviously superior to the pseudoinviscid expression[1] shown as well.

Two points of the experimental data set (x, Δp_1) have been used to determine the parameters $A_1 = 13.30$ (integration constant) and $b_1 = 0.03805$; this is necessary since no physical input is available regarding values of the injection velocity perturbation B_1. The same data set is correlated by Eq. (68) as well, leading to

$$\Delta p_1 = b_3[1-\sqrt{1-(b_4 x)^2}]$$

$$b_3 \equiv (b_2/\lambda_0)^{1/2} \tag{70}$$

and the correlation parameters are $b_3 = 55.45$ and $b_4 = 0.01674$. In both cases, the same arbitrary pressure drop scale was used to facilitate overplotting with the original data points of Brown et al.[8]

At each axial position x, the data points plotted by Brown et al. in Fig. 3 obtain a slight vertical spread. The different symbols used actually correspond to distinct injection Reynolds numbers and Mach numbers (R_{e0}, M_0) as shown in the accompanying table. The aforementioned vertical spread is caused mainly by the differences in the R_{e0} and M_0 parameters, not by experimental error. Once these differences are accounted for, the actual consistency of the experimental data can be demonstrated; in Fig. 4, this consistency is shown to be much better than what might be inferred from Fig. 3.

In Fig. 4, two of the original data sets are reproduced, corresponding to dark squares (low R_{e0}) and light circles (high R_{e0}) in Fig. 3. The axial pressure drop data are first rescaled, multiplying through by the appropriate conversion factor,

$$CF \equiv \frac{\gamma M_0^2/2}{\epsilon} = \frac{\epsilon}{2K_m}$$

for each data set. With the proper scaling used in Fig. 4, the sensitivity of the normalized axial pressure drop data to the Reynolds number (and the parameter K_m) is demonstrated. The cosine pressure drop formula of Eq. (69) is used to correlate each of the two data sets in Fig. 4 (separately using two sets of parameters A_1 and b_1) with excellent results.

Two important observations can now be made:

1) The axial pressure drop to lowest order is $\mathcal{O}(\epsilon)$ and is governed by the dissipative wall-layer processes, as derived in the present analysis. The x dependence of both cosine and square root solutions obtained herein [Eqs. (69) and (70)] seems different from the Culick expression[1]; however, both have parabolic leading terms when expanded for small $(b_1 x)$ and $(b_4 x)$, respectively.

2) One need not invoke turbulence generation in the main flow to explain the departure of the measured axial pressure drop from that predicted by the pseudoinviscid solution of Culick.[1] The correction obtained to the parabolic expression[1] is not negligible: at $x = 32$, it amounts to 17%, as shown in Fig. 3.

Another property of interest is the wall friction coefficient, or dimensionless wall shear stress,

$$C_f = \frac{\tau_w^*}{\frac{1}{2}\rho^* \bar{u}^{*2}} = \mu^* \frac{\partial u^*}{\partial y^*} \Big/ \frac{1}{2}\rho^* \bar{u}^{*2}$$

where $\bar{u}^*$ denotes the mean axial core flow velocity. Using the dimensionless convention employed herein, along with the wall-layer coordinate,

$$C_{f0} = \epsilon \frac{\partial u_0}{\partial y} \Big/ 2x^2 \tag{71}$$

as $\bar{u} = 2x$ was used for a cylindrical port and subscript zero denotes zeroth-order convention. Now, from Eqs. (28) and (64),

$$C_{f0} = \frac{\epsilon}{2} K_m b_1 A_1 \frac{(\sin b_1 x)}{x^2} \tag{72}$$

This parameter is plotted against $1/2x$ (which denotes the ratio of blowing of mean axial velocity) in Fig. 5. A nearly linear relationship is obtained, using the coefficient values obtained from the two data groups in Fig. 4. In comparison, the data obtained by Olson and Eckert[6] is considered. Reference 6 includes a plot of the ratio of (axial pressure gradient)/(mean dynamic axial head) vs $v_0^*/u_0^* = 1/2x$. This obtains an almost linear correlation, as would be expected from a parabolic pressure drop. However, the slight curvature particularly apparent at small values of $1/2x < 0.01$ can be followed only with the present formulation and not with any purely parabolic pressure profile. Thus, the first-order pressure distribution obtained from the viscous wall-layer analysis agrees well with the measured data of Brown et al.,[8] while the associated wall friction coefficient follows the same trend as that measured by Olson and Eckert.[6]

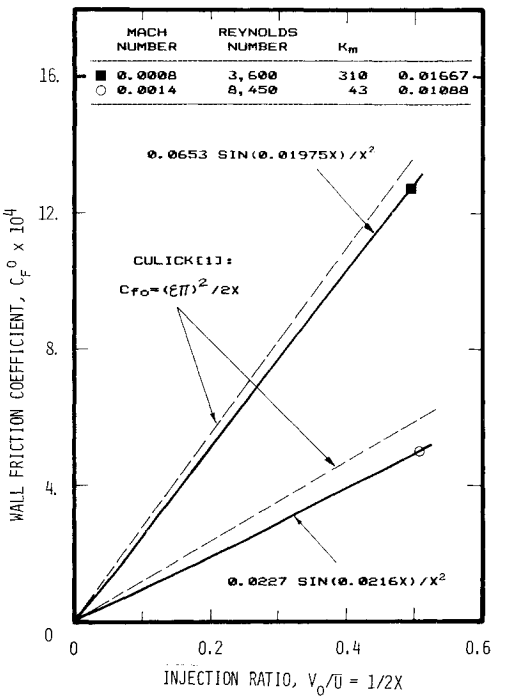

Fig. 5 Viscous friction coefficient calculated for the two cases shown in Fig. 4. The deviation (slight curvature) from linear behavior at large values of x is in agreement with the measurements of Olson and Eckert[6] and could not be supported by the rotational-inviscid theory.

Conclusions

A derivation of the viscous wall-layer regime has been presented, pertaining to injected flow in a cylindrical porous tube, in simulation of interior solid-propellant rocket flows.

Solutions for the radial coordinate (or y dependence) of all the dependent variables up to the first order have been generated in polynomial form. The (x,t) dependence is defined in terms of a relatively simple partial differential system.

Particular steady-state results of the analysis are:

1) The first-order axial pressure drop was solved in terms of the viscous wall-layer processes, using a general injection perturbation function for the porous wall. The analytical expressions obtained are in very good agreement with the experimental cold-flow data of Brown et al.[8] regarding the axial pressure drop.

2) The variation of the axial velocity profile $u_0(x,y) + \epsilon u_1(x,y)$ within the injected wall layer was also solved. The zeroth-order axial velocity distribution within the wall layer is linear radially; thus, $\partial^2 u_0/\partial y^2 = 0$ and to lowest-order viscous dissipation is negligible in the axial momentum balance. This may explain why rotational, inviscid solutions such as that of Culick[1] and others (chosen to satisfy the no-slip condition near the wall) obtain such good zeroth-order approximations.

Certain difficulties in simulating internal rocket flows by injected porous pipe flows have been pinpointed. Of particular concern is the pressure sensitivity of the perturbed wall injection rate, which is of opposite signs for porous

materials and for propellants. At steady state, this is shown to affect the axial pressure distribution; through the gradient, dp_1/dx, the vorticity generation rate within the wall layer is therefore expected to differ between the injected porous pipe and internal rocket flows. Despite these drawbacks, cold-flow simulation still contains all of the necessary fluid dynamic mechanisms prevailing in the rocket motor. For this reason, it remains a valid simulative tool.

The good agreement between the foregoing analytical results and the experimental data indicates that the viscous wall-layer approach developed herein is physically valid and obtains a significant effect over a considerable portion of the axial length of the injected pipe. Therefore, the present work can be considered to be a necessary preliminary step toward nonsteady analysis of viscoacoustic coupling in this family of injected flows.

Acknowledgment

This study was supported by the U. S. Air Force Office of Scientific Research, Contract F49620-81-C-0018. Technical cognizance was provided by Dr. Leonard H. Caveny.

References

[1]Culick, F. E. C., "Rotational, Axisymmetric Mean Flow and Damping of Acoustic Waves in a Solid Propellant Rocket," *AIAA Journal*, Vol. 4, Aug. 1966, pp. 1462-1464.

[2]Berman, A. S., "Laminar Flow in Channels with Porous Walls," *Journal of Applied Physics*, Vol. 24, Sept. 1953, pp. 1232-1235.

[3]Taylor, G., "Fluid Flow in Regions Bound by Porous Surfaces," *Proceedings of the Royal Society of London*, Ser. A, Vol. 234, No. 1199, 1956, pp. 456-475.

[4]Wageman, W. E. and Guevara, F. A., "Fluid Flow Through a Porous Channel," *Physics of Fluids*, Vol. 3, Nov.-Dec. 1960, pp. 878-881.

[5]Dunlap, R., Willoughby, P. G., and Hermsen, R. W., "Flowfield in the Combustion Chamber of a Solid Propellant Rocket Motor," *AIAA Journal*, Vol. 12, Oct. 1974, pp. 1440-1442.

[6]Olson, R. M. and Eckert, E. R. G., "Experimental Studies of Turbulent Flow in a Porous Circular Tube with Uniform Fluid Injection Through the Tube Walls," *Journal of Applied Mechanics, Transactions of ASME*, March 1966, pp. 7-17.

[7]Huesman, K. and Eckert, E. R. G., "Studies of the Laminar Flow and Transition to Turbulence in Porous Tubes, with Uniform Injection Through the Tube Wall," (translation), *Warme und Stoffübertrannung*, Vol. 1, 1968, pp. 2-9.

[8]Brown, R. S., Waugh, R. C., Willoughby, P. G., and Dunlap, R., "Coupling Between Velocity Oscillations and Solid Propellant Combustion," *19th JANNAF Combustion Meeting*, CPIA Pub. 366, Vol. I, 1968, pp. 191-208.

[9]Yagodkin, V. I., "Use of Channels with Porous Walls for Studying Flows Which Occur During Combustion of Solid Propellants," *Proceedings of 18th Aeronautics Congress (USSR)*, Vol. 3, 1967, pp. 69-79 (translation).

[10]Yamada, K., Goto, M., and Ishikawa, N., "Simulative Study on the Erosive Burning of Solid Rocket Motors," *AIAA Journal*, Vol. 14, 1976, pp. 1170-1177.

[11]Varapaev, V. N. and Yagodkin, V. I., "Flow Instability in a Channel with Porous Walls," *Izvestiya Akademii Nauk SSSR, Mekhanika Zhidkosti i Gaza*, Vol. 4, No. 5, 1969, pp. 91-95 (translation).

[12]Sviridenkov, A. A. and Yagodkin, V. I., "Flow in the Initial Sections of Channels with Permeable Walls," *Izvestiya Akademii Nauk SSSR, Mekhanika Zhidkosti i Gaza*, No. 5, Sept.-Oct. 1976, pp. 43-48 (translation).

[13]Goldshtik, M. A. and Sapozhnikov, V. A., "Laminar Flow Stability in a Mass Force Field," *Izvestiya Akademii Nauk SSSR, Mekhanika Zhidkosti i Gaza*, Vol. 3, No. 5, 1968, pp. 42-46.

[14]Alekseev, Y. N. and Korotkin, A. I., "Effect of Transverse Stream Velocity in an Incompressible Boundary Layer on the Stability of the Laminar Flow Regime," *Izvestiya Akademii Nauk SSSR, Mekhanika Zhidkosti i Gaza*, Vol. 1, No. 1, 1966, pp. 32-36.

[15]Flandro, G. A., "Nonlinear Time Dependent Combustion of a Solid Rocket Propellant," *Proceedings of 19th JANNAF Combustion Meeting*, CPIA Pub. 366, Vol. II, Oct. 1982, pp. 111-122.

[16]T'ien, J., "Oscillatory Burning of Solid Propellants including Gas Phase Time Lag," *Combustion Science and Technology*, Vol. 5, 1972, pp. 47-54.